Utilizing Multiple Subpixel Shifted Images in Subpixel Mapping With Image Interpolation

Qunming Wang and Wenzhong Shi

***Abstract*—In this letter, multiple subpixel shifted images (MSIs) were utilized to increase the accuracy of subpixel mapping (SPM), based on the fast bilinear and bicubic interpolation. First, each coarse spatial resolution image of MSI is soft classified to obtain class fraction images. Using bilinear or bicubic interpolation, all fraction images of MSI are upsampled to the desired fine spatial resolution. The multiple fine spatial resolution images for each class are then integrated. Finally, the integrated fine spatial resolution images are used to allocate hard class labels to subpixels. Experiments on two remote sensing images showed that, with MSI, both bilinear and bicubic interpolation-based SPMs are more accurate. The new methods are fast and do not need any prior spatial structure information.**

***Index Terms*—Image interpolation, remote sensing, subpixel mapping (SPM), subpixel shifted images, superresolution mapping.**

I. Introduction

LAND cover mapping from remote sensing images is always accomplished by classification. The conventional hard classification assigns each pixel to a single land cover class. However, this is insufficient for interpretation of mixed pixels, which contain more than one class. Mixed pixels are a common phenomenon in remote sensing images. Soft classification has been developed to estimate the fractions of classes within mixed pixels but fails to predict the spatial distribution of classes. Subpixel mapping (SPM; also termed superresolution mapping or downscaling in remote sensing) is a technique to extract land cover information at the subpixel scale [1] by transforming the outputs of soft classification (i.e., fractions of classes) to finer resolution maps. The fractions are used as a constraint in the SPM problem.

SPM is usually performed based on spatial dependence theory; compared with more distant pixels, neighboring pixels are more likely to be of the same class. Over the past decade, various algorithms have been developed to tackle the SPM problem, such as pixel swapping algorithm (PSA) [2]–[5], genetic algorithms [6], Hopfield neural network [7], [8], Markov random field [9]–[12], back-propagation neural network [13], and indicator cokriging [14], [15]. Some of them are time-consuming as they require several iterations to approach satisfactory SPM results (e.g., genetic algorithms, Hopfield neural network, and Markov random field), while other algorithms need prior spatial structure information to build models for classes (e.g., back-propagation neural network and indicator cokriging).

SPM can be achieved simply by estimating soft class attribute values (between 0 and 1 for each class) at a desired fine spatial resolution first and then hardening the values to fine class labels (0 or 1 for each class) [16], [17]. The soft class attribute values indicate the probabilities of class occurrence at subpixels. The prediction of those values is a critical step in SPM, which is the core idea of some existing SPM algorithms, including the Hopfield neural network, back-propagation neural network, and indicator cokriging. The critical step can also be realized by some image superresolution algorithms, and in this letter, the classical bilinear and bicubic interpolation algorithms are used for this purpose. The advantages of bilinear and bicubic interpolation are that both of them are nonparametric, noniterative, and fast algorithms. Moreover, they do not need prior spatial structure information on classes.

SPM is widely known as an underdetermined problem. The performances of many SPM approaches are limited by the inherent uncertainty in SPM. Recently, additional information from auxiliary data sets has been applied to decrease the uncertainty in SPM and to increase the SPM accuracy [18]–[23]. In this letter, multiple subpixel shifted images (MSIs) are used as auxiliary data sets. These images can be captured by sensors that cover the same area periodically. This type of data set has been used for enhancement of SPM in [20]–[23]. Unlike the methods in [20]–[23] which are iteration based or need prior information, the methods studied in this letter inherit the aforementioned advantages of bilinear and bicubic interpolation.

The remainder of this letter is organized as follows. In Section II, the principles of the bilinear and bicubic interpolation-based SPM methods are introduced, followed by details of utilizing MSI in them. Section III gives the experimental results, and the conclusion is drawn in Section IV.

II. Methods

Suppose that the soft classification results of a coarse spatial resolution image are K (K is the number of land cover classes) fraction images $\mathbf{F}_1, \mathbf{F}_2, \ldots, \mathbf{F}_K$, and each coarse pixel is divided into $S \times S$ subpixels. Let P_j ($j = 1, 2, \ldots, M$, M is the number of pixels in the coarse image) be a coarse pixel, $p_i (i = 1, 2, \ldots, MS^2)$ be a subpixel, and $F_k(P_j)$ is the fraction of the kth class for pixel P_j.

Manuscript received April 24, 2013; revised July 13, 2013; accepted August 17, 2013. Date of publication September 9, 2013; date of current version December 2, 2013. This work was supported by the Research Grants Council, Hong Kong (PolyU 5249/12E), and The Hong Kong Polytechnic University (Project Nos. 1-ZV4F, 1-ZVBA, G-U753, G-UA35, G-YK75, G-YJ75, G-YZ26, and H-ZG77). *(Corresponding author: W. Shi.)*

The authors are with the Department of Land Surveying and Geo-Informatics, The Hong Kong Polytechnic University, Kowloon, Hong Kong (e-mail: wqm11111@126.com; lswzshi@polyu.edu.hk).

Color versions of one or more of the figures in this paper are available online at http://ieeexplore.ieee.org.

Digital Object Identifier 10.1109/LGRS.2013.2279138

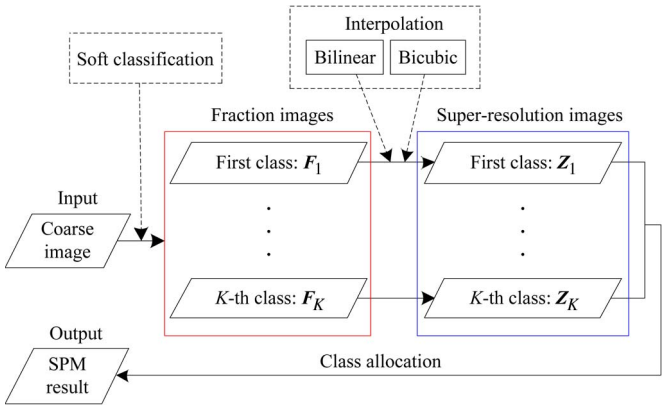

Fig. 1. Flowchart of the bilinear and bicubic interpolation-based SPMs.

A. Bilinear and Bicubic Interpolation-Based SPMs

Let $Z_k(p_i)$ be the soft attribute value for the kth class at subpixel p_i. Taking the fraction images $\mathbf{F}_1, \mathbf{F}_2, \ldots, \mathbf{F}_K$ as inputs, both bilinear and bicubic interpolation can produce superresolution images $\mathbf{Z}_1, \mathbf{Z}_2, \ldots, \mathbf{Z}_K$ quickly, each of which are composed of MS^2 soft attribute values.

In the SPM problem, the fractions and zoom factor S are used to determine the number of subpixels belonging to each class. More specifically, within each coarse pixel P_j, the number of subpixels for the kth class $NC_k(P_j)$ is

$$NC_k(P_j) = \text{round}\left(F_k(P_j)S^2\right) \tag{1}$$

where round $(\bullet)$ is a function that takes the integer nearest to $\bullet$.

Along with the constraints in (1), $Z_1, Z_2, \ldots, Z_K$ are used to allocate hard class labels to subpixels. In this letter, a class allocation method in [17] is employed, with which subpixels for each class are allocated in turn. For each class, subpixels with larger soft attribute values are allocated before those with smaller ones. Using this method, the autocorrelation for each class can be maximized. The visiting order of all classes can be decided by comparing Moran's I [3] of K classes, and the classes with higher indices are visited first. Fig. 1 is the flowchart describing the bilinear and bicubic interpolation-based SPM methods.

B. Using MSI in Bilinear and Bicubic Interpolation-Based SPMs

MSI can be acquired by a satellite taking images over the same area at different times. The images usually have the same spatial resolution. Due to the slight relative translations between the satellite and Earth, these images will not be completely identical and will usually be shifted from each other. In this letter, the MSIs are assumed to be translated horizontally and vertically at the subpixel level.

Suppose that the number of MSI is R, and the subpixel shift between the rth $(r = 1, 2, \ldots, R)$ and the first coarse image is (x_r, y_r), which indicates that the rightward and downward shifts are x_r and y_r subpixels. If the coordinate of a subpixel, e.g., p_i, in the first image is (a_m, b_m), the coordinate of its corresponding subpixel p_i^r in the rth coarse image should be $(a_m - x_r, b_m - y_r)$. An example is given in Fig. 2 to illustrate the subpixel shifts. There are two 3×3 coarse images A (black) and B (red). Suppose that each coarse pixel in the two images is

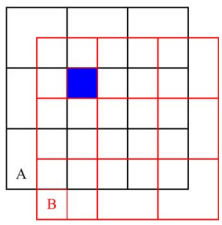

Fig. 2. Two coarse images A and B with subpixel shift (1, 1).

divided into 2×2 subpixels $(S = 2)$. The subpixel shift from A to B is (1, 1). If a subpixel, labeled in blue in the figure, is at (3, 3) in A, then it should be at (2, 2) in B.

In the proposed bilinear and bicubic interpolation-based SPMs with MSI, the soft attribute value for the kth class at subpixel p_i is determined by integration of R attribute values

$$Z_k(p_i) = \frac{1}{R}\sum_{r=1}^{R} Z_k\left(p_i^r\right) \tag{2}$$

where $Z_k(p_i^r)$ indicates the soft attribute value for the kth class at p_i's corresponding subpixel p_i^r in the rth coarse image. $Z_k(p_i^r)$ is estimated by bilinear or bicubic interpolation, taking the kth class fraction image for the rth coarse image as input.

C. Implementation of the Proposed Methods

The implementation of the bilinear and bicubic interpolation-based SPMs with MSI includes five steps.

- Step 1) Estimation of subpixel shifts (x_r, y_r) $(r = 1, 2, \ldots, R)$. Many existing algorithms can be applied to estimate the subpixel shift, such as phase correlation and cross-correlation matching.
- Step 2) Soft classification of MSI. All R coarse images are soft classified. The results for each coarse image are K class fraction images. Correspondingly, there are R fraction images for each class.
- Step 3) Image interpolation of fraction images. With bilinear or bicubic interpolation, all RK coarse images are superresolved to the desired fine spatial resolution. The outputs are RK superresolution images.
- Step 4) Integration of interpolated images. For each class, its R interpolated superresolution images are integrated [see (2)]. In this way, K fine spatial resolution images will be generated.
- Step 5) Class allocation for each subpixel. Under the constraints in (1), K fine spatial resolution images generated in step 4 are used for allocation of hard class labels, and subpixels for each class are allocated in turn. Details of the class allocation method can be found in [17].

In this letter, the method for utilizing MSI for enhancement of SPM is different from that in [20]–[22]. In [20]–[22], additional information from MSI is used at coarse spatial resolution. Specifically, R (the number of MSI) constraints at original coarse pixel scale, such as those in terms of class fraction [20], [22] or spectral reflectance of the coarse pixel [21], are incorporated into the relevant SPM models. In the SPM process, each subpixel corresponds to R coarse pixels in MSI and has to satisfy R constraints when its class attribute is predicted. As the class attribute of each subpixel varies after each prediction,

iterations are required to approach optimal SPM results. The whole process is always time-consuming. In the proposed methods, however, information from MSI is exploited at subpixel scale by upsampling all fraction images of MSI to the desired fine spatial resolution in advance (see step 3). The interpolated images for MSI are then straightforwardly integrated, which is a noniterative and very fast scheme.

Superresolution for each image of MSI is accomplished by bilinear or bicubic interpolation. The two interpolation algorithms are well known for their simplicity and high computational efficiency. They are nonparametric and noniterative and can process coarse spatial resolution images without prior spatial structure information. Based on bilinear and bicubic interpolation, therefore, the new SPM methods inherit all their advantages, and MSI data are utilized efficiently.

III. Experiments

Experiments on two remote sensing images were carried out to validate the proposed SPM methods. Five SPM methods were tested and compared: PSA, bilinear, bicubic, bilinear with MSI, and bicubic with MSI. All experiments were tested on an Intel Core 2 Processor (1.80-GHz Duo central processing unit, 2.00-GB random access memory) with MATLAB 7.1 version.

For supervised assessment of SPM methods, fine spatial resolution images were degraded via a mean filter to simulate coarse images. The task of SPM was to restore the fine spatial resolution map. Since many algorithms can be used for image registration of MSI, the estimation of subpixel shifts is beyond the scope of this letter. To solely concentrate on the performance of the proposed SPM methods, in each experiment, the fine spatial resolution image was first shifted and then degraded to generate the MSI. In experiment 1 and experiment 2, four shifted images were considered, and the subpixel shifts were assumed to be (0, 0), (0.5, 0), (0, 0.5), and (0.5, 0.5) coarse pixel. The number of MSI is further discussed in Section III-C.

The accuracy of SPM was evaluated quantitatively by the overall accuracy in terms of the percentage of correctly classified pixels (PCC). McNemar's test was also applied to determine whether the difference between the SPM results is statistically significant. Using the 95% degree of confidence level, the difference is considered to be statistically significant if the calculated z-value is greater than 1.96.

A. Experiment 1

In the first experiment, an aerial image covering an area in Bath, U.K., was used for the test. Fig. 3(a) shows the image, while Fig. 3(b) shows the reference land cover map, which was provided by Dr. A. J. Tatem. The image has 360 × 360 pixels, with a pixel size of 0.6 m × 0.6 m, and covers four classes: road, tree, building, and grass. The reference map in Fig. 3(b) was degraded with a 10 × 10 mean filter to generate fraction images for classes, each of which has 36 × 36 coarse pixels.

The SPM results of bilinear, bicubic, bilinear with MSI, and bicubic with MSI are shown in Fig. 3(c)–(f). As can be seen in Fig. 3(c) and (d), with respect to the restoration of the road class, there are obvious disconnected shapes; as for trees and buildings, many burrs occur on their boundaries, which seem rough. With the aid of MSI, the performances of both bilinear and bicubic interpolation-based SPM methods are noticeably

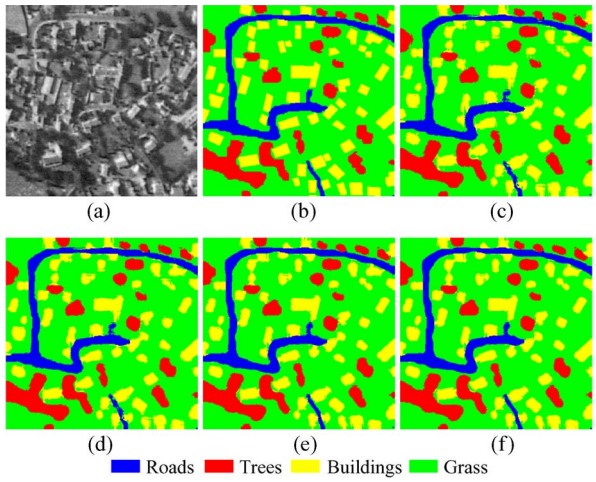

Fig. 3. SPM results for the aerial image. (a) Aerial image. (b) Reference land cover map. (c) Bilinear result. (d) Bicubic result. (e) Bilinear with MSI result. (f) Bicubic with MSI result.

TABLE I
Accuracy (in Percent) of SPM Methods for the Aerial Image ($S = 10$)

	PSA	Bilinear	Bicubic	Bilinear with MSI	Bicubic with MSI
Road	93.94	94.17	94.44	96.88	96.98
Tree	92.71	92.60	92.90	94.05	94.31
Building	87.79	86.45	87.12	89.86	90.34
Grass	91.46	90.96	91.35	93.28	93.58
PCC	91.01	90.44	90.87	92.96	93.27

improved. In Fig. 3(e) and (f), the spatial continuity of each class is greater, the boundaries of the classes are smoother, and the results are closer to the reference map in Fig. 3(b).

Table I gives the accuracy of each class and the overall accuracy in terms of PCC for five SPM methods. In this experiment, the nonmixed pixels were not considered in the accuracy statistics because these pixels will only increase the accuracy without providing any useful information on the performance of the SPM methods [5], [6]. As shown in Table I, PSA produces a greater PCC than both bilinear and bicubic methods in experiment 1. Comparing the accuracy of the four interpolation-based methods, using MSI, the SPM accuracy of bilinear and bicubic methods is evidently enhanced and also higher than that for PSA. For the proposed two methods with MSI, the SPM accuracy of road, tree, building, and grass increases by around 2.5%, 1.5%, 3%, and 2%, respectively, when compared to the bilinear and bicubic methods. For the two classes, road and building, they are regularly distributed and mainly appear within objects which have straight lines and right angles in the studied area. Hence, increases in the accuracy with which they are predicted are more obvious than those for the other two classes. The PCC of the bilinear method increases from 90.44% to 92.96% when MSIs are used, and for the bicubic method, the PCC increases from 90.87% to 93.27% when MSIs are used. The McNemar's test indicates that the PCCs of both bilinear with MSI and bicubic with MSI are significantly higher than those for the PSA, bilinear, and bicubic methods. In addition, bicubic with MSI achieves significantly higher accuracy than the other four SPM methods.

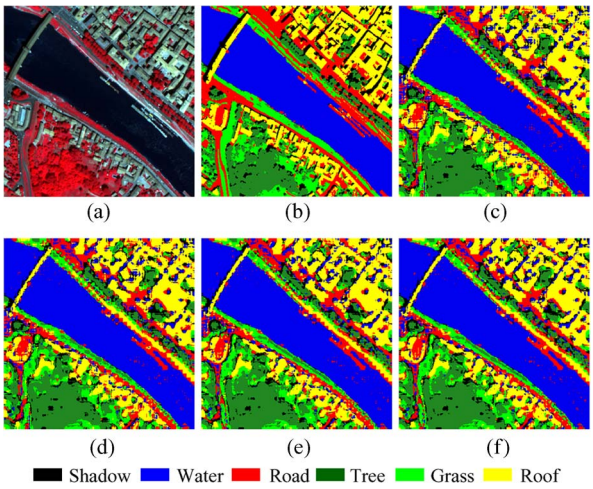

Fig. 4. SPM results for the ROSIS image. (a) Three-band color image of the ROSIS hyperspectral data set (bands 102, 56, and 31 as RGB). (b) Reference land cover map. (c) Bilinear result. (d) Bicubic result. (e) Bilinear with MSI result. (f) Bicubic with MSI result.

TABLE II
CC OF SOFT CLASSIFICATION RESULTS FOR THE DEGRADED 10-m ROSIS IMAGE

Shadow	Water	Road	Tree	Grass	Roof
0.7668	0.9617	0.8518	0.9426	0.8797	0.8854

B. Experiment 2

In this experiment, a hyperspectral image was studied. The image was acquired by the Reflective Optics System Imaging Spectrometer (ROSIS) sensor during a flight campaign over Pavia, northern Italy. It has a spatial resolution of 1.3 m with 102 bands. The tested region has 384 × 384 pixels and mainly covers six classes: shadow, water, road, tree, grass, and roof. The false color image is shown in Fig. 4(a). Fig. 4(b) gives the reference land cover map of the 1.3-m hyperspectral image, which was obtained with the tensor discriminative locality alignment-based classifier in [24]. A 10-m spatial resolution image was created by degrading the original 1.3-m hyperspectral image band by band via an 8 × 8 mean filter. The fine spatial resolution land cover map in Fig. 4(b) was used for both visual and quantitative assessments, which has an overall accuracy of 96.42% for 5343 test samples and provides a reliable reference data set.

Soft classification was implemented on the 10-m coarse image first to obtain the fraction images. Fully constrained least squares linear spectral mixture analysis [25] was employed for soft classification, considering its simple physical meaning and convenience in application. The predicted fraction is compared to the reference fraction by means of the correlation coefficient (CC), as exhibited in Table II. The reference fraction data were acquired by degrading Fig. 4(b) with an 8 × 8 pixel mean filter. We can observe that the water, tree, and roof classes have higher CCs than the other three classes, suggesting that the soft classification of water, tree, and roof is more accurate.

The bilinear, bicubic, bilinear with MSI, and bicubic with MSI methods were applied to the predicted fraction images, with $S = 8$, generating the 1.3-m land cover maps shown in Fig. 4(c)–(f). It can be observed that many linear artifacts exist in the bilinear and bicubic results. Using MSI, the phenomenon is alleviated, and the SPM results are more in agreement with the reference map in Fig. 4(b). The SPM accuracy of the four methods as well as PSA is listed in Table III. Due to the low soft classification accuracy of shadow, road, and grass, as seen in Table II, the SPM accuracy of these three classes is relatively lower in comparison with the other three classes. When compared to the SPM accuracy in the first experiment, the accuracy of all five methods is much lower in this experiment. This is attributed to the errors from soft classification as well as the more complex spatial pattern in the studied area. Intercomparison of the values in Table III reveals that, with MSI, both bilinear and bicubic methods achieve higher SPM accuracy for all six classes than the PSA, bilinear, and bicubic methods. The McNemar's test suggests that bilinear with MSI and bicubic with MSI methods have significantly higher PCCs than the PSA, bilinear, and bicubic methods.

TABLE III
ACCURACY (IN PERCENT) OF SPM METHODS FOR THE ROSIS IMAGE ($S = 8$)

	PSA	Bilinear	Bicubic	Bilinear with MSI	Bicubic with MSI
Shadow	34.68	34.33	34.82	37.37	37.99
Water	96.22	96.28	96.32	96.45	96.52
Road	48.51	48.57	48.86	50.99	51.39
Tree	76.07	75.67	76.07	77.61	77.90
Grass	54.48	53.27	53.51	56.06	56.33
Roof	76.20	76.43	76.74	78.89	79.21
PCC	70.09	69.91	70.17	71.75	72.04

TABLE IV
SUBPIXEL SHIFTS FOR DISCUSSION ON THE NUMBER OF MSI

Number of images	Sub-pixel shifts
2	(0,0) (3,0)
4	(0,0) (3,0) (0,3) (3,3)
6	(0,0) (3,0) (6,0) (0,3) (3,3) (6,3)
9	(0,0) (3,0) (6,0) (0,3) (3,3) (6,3) (0,6) (3,6) (6,6)

In experiment 1, the bilinear and bicubic methods took around 2 s, while the proposed methods took less than 5 s. In experiment 2, the bilinear and bicubic methods took less than 4 s, whereas the proposed methods took less than 8 s. For PSA running with 20 iterations, however, it took 90 and 138 s in experiment 1 and experiment 2.

C. Analysis of the Number of MSI

The proposed SPM methods were tested with different numbers of MSI. We discussed four numbers: 2, 4, 6, and 9. The corresponding subpixel shifts are shown in Table IV. Note that, when four images were discussed here, the subpixel shifts are different from those in the previous two experiments. The impact of the number of MSI can be seen in Fig. 5. For both aerial and ROSIS images, when the number of MSI increases from 1 to 9, the PCCs of both the bilinear and bicubic methods increase. Moreover, the bicubic method consistently obtains a higher PCC than the bilinear method.

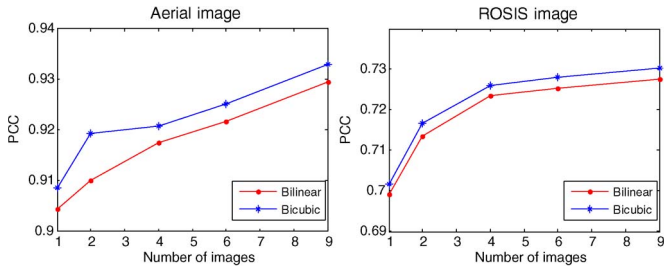

Fig. 5. Influence of the number of subpixel shifted images for bilinear and bicubic interpolation-based SPMs.

IV. Conclusion

SPM is always an underdetermined problem. In this letter, MSIs were used as additional information to enhance SPM, which is achieved by fast and simple bilinear and bicubic interpolation. The MSIs were subpixel shifted from each other, situation replicated by sensors taking images over the same area at different times. Similar to original bilinear and bicubic interpolation-based SPMs, the proposed methods are free of iteration and very fast, and do not need prior spatial structure information.

Two remote sensing images were tested in the experiments for validation of the proposed SPM methods. Both visual and quantitative assessments showed that the new methods can noticeably increase the accuracy of conventional bilinear and bicubic interpolation-based SPMs. The SPM results of the new methods are visually more continuous and smoother than those obtained without MSI. The PCCs of the new methods are significantly higher than those of conventional methods. Furthermore, the proposed SPM methods took only several seconds for the two studied images. The considerably low computational burden fully indicates that the proposed methods are fast methods to utilize MSI in SPM. Therefore, the proposed methods show their great potential in real-time applications and in cases where prior spatial structure information is unavailable. In the future research, additional information from other auxiliary data sets will be utilized in image interpolation-based SPM.

Acknowledgment

The authors would like to thank Prof. P. M. Atkinson of the University of Southampton, Southampton, U.K., for his careful proofreading as well as helpful suggestions, Dr. A. J. Tatem of the University of Southampton for providing the aerial image and its land cover map, Prof. P. Gamba of the University of Pavia, Pavia, Italy, for providing the ROSIS data, Dr. L. Zhang of Wuhan University, Wuhan, China, for providing the land cover map of the ROSIS data, and the handling editor and anonymous reviewers for their valuable comments.

References

[1] P. M. Atkinson, "Downscaling in remote sensing," *Int. J. Appl. Earth Observ. Geoinf.*, vol. 22, pp. 106–114, Jun. 2013.

[2] P. M. Atkinson, "Sub-pixel target mapping from soft-classified, remotely sensed imagery," *Photogramm. Eng. Remote Sens.*, vol. 71, no. 7, pp. 839–846, Jul. 2005.

[3] Y. Makido, A. Shortridge, and J. P. Messina, "Assessing alternatives for modeling the spatial distribution of multiple land-cover classes at sub-pixel scales," *Photogramm. Eng. Remote Sens.*, vol. 73, no. 8, pp. 935–943, Aug. 2007.

[4] A. Villa, J. Chanussot, J. A. Benediktsson, C. Jutten, and R. Dambreville, "Unsupervised methods for the classification of hyperspectral images with low spatial resolution," *Pattern Recognit.*, vol. 46, no. 6, pp. 1556–1568, Jun. 2013.

[5] Q. Wang, L. Wang, and D. Liu, "Particle swarm optimization-based sub-pixel mapping for remote-sensing imagery," *Int. J. Remote Sens.*, vol. 33, no. 20, pp. 6480–6496, Oct. 2012.

[6] K. C. Mertens, L. P. C. Verbeke, E. I. Ducheyne, and R. De Wulf, "Using genetic algorithms in sub-pixel mapping," *Int. J. Remote Sens.*, vol. 24, no. 21, pp. 4241–4247, Nov. 2003.

[7] A. J. Tatem, H. G. Lewis, P. M. Atkinson, and M. S. Nixon, "Super-resolution target identification from remotely sensed images using a Hopfield neural network," *IEEE Trans. Geosci. Remote Sens.*, vol. 39, no. 4, pp. 781–796, Apr. 2001.

[8] A. M. Muad and G. M. Foody, "Impact of land cover patch size on the accuracy of patch area representation in HNN-based super resolution mapping," *IEEE J. Sel. Topics Appl. Earth Observ. Remote Sens.*, vol. 5, no. 5, pp. 1418–1427, Oct. 2012.

[9] T. Kasetkasem, M. K. Arora, and P. K. Varshney, "Super-resolution land-cover mapping using a Markov random field based approach," *Remote Sens. Environ.*, vol. 96, no. 3/4, pp. 302–314, Jun. 2005.

[10] V. A. Tolpekin and A. Stein, "Quantification of the effects of land-cover-class spectral separability on the accuracy of Markov-random-field based superresolution mapping," *IEEE Trans. Geosci. Remote Sens.*, vol. 47, no. 9, pp. 3283–3297, Sep. 2009.

[11] J. P. Ardila, V. A. Tolpekin, W. Bijker, and A. Stein, "Markov-random-field-based super-resolution mapping for identification of urban trees in VHR images," *ISPRS J. Photogramm. Remote Sens.*, vol. 66, no. 6, pp. 762–775, Nov. 2011.

[12] X. Li, Y. Du, and F. Ling, "Spatially adaptive smoothing parameter selection for Markov random field based sub-pixel mapping of remotely sensed images," *Int. J. Remote Sens.*, vol. 33, no. 24, pp. 7886–7901, Dec. 2012.

[13] D. Nigussie, R. Zurita-Milla, and J. G. P. W. Clevers, "Possibilities and limitations of artificial neural networks for subpixel mapping of land cover," *Int. J. Remote Sens.*, vol. 32, no. 22, pp. 7203–7226, Nov. 2011.

[14] A. Boucher, P. C. Kyriakidis, and C. Cronkite-Ratcliff, "Geostatistical solutions for super-resolution land cover mapping," *IEEE Trans. Geosci. Remote Sens.*, vol. 46, no. 1, pp. 272–283, Jan. 2008.

[15] H. Jin, G. Mountrakis, and P. Li, "A super-resolution mapping method using local indicator variograms," *Int. J. Remote Sens.*, vol. 33, no. 24, pp. 7747–7773, Dec. 2012.

[16] F. Ling, Y. Du, X. Li, W. Li, F. Xiao, and Y. Zhang, "Interpolation-based super-resolution land cover mapping," *Remote Sens. Lett.*, vol. 4, no. 7, pp. 629–638, Jul. 2013.

[17] Q. Wang, W. Shi, and L. Wang, "Allocating classes for soft-then-hard sub-pixel mapping algorithms in units of class," *IEEE Trans. Geosci. Remote Sens.*, vol. 52, no. 5, pp. 2940–2952, May 2014.

[18] G. M. Foody, "Sharpening fuzzy classification output to refine the representation of sub-pixel land cover distribution," *Int. J. Remote Sens.*, vol. 19, no. 13, pp. 2593–2599, Sep. 1998.

[19] M. Q. Nguyen, P. M. Atkinson, and H. G. Lewis, "Super-resolution mapping using Hopfield neural network with panchromatic imagery," *Int. J. Remote Sens.*, vol. 32, no. 21, pp. 6149–6176, Nov. 2011.

[20] F. Ling, Y. Du, F. Xiao, H. Xue, and S. Wu, "Super-resolution land-cover mapping using multiple sub-pixel shifted remotely sensed images," *Int. J. Remote Sens.*, vol. 31, no. 19, pp. 5023–5040, Oct. 2010.

[21] L. Wang and Q. Wang, "Subpixel mapping using Markov random field with multiple spectral constraints from subpixel shifted remote sensing images," *IEEE Geosci. Remote Sens. Lett.*, vol. 10, no. 3, pp. 598–602, May 2013.

[22] X. Xu, Y. Zhong, L. Zhang, and H. Zhang, "Sub-pixel mapping based on a MAP model with multiple shifted hyperspectral imagery," *IEEE J. Sel. Topics Appl. Earth Observ. Remote Sens.*, vol. 6, no. 2, pp. 580–593, Apr. 2013.

[23] Q. Wang, W. Shi, and L. Wang, "Indicator cokriging-based subpixel land cover mapping with shifted images," *IEEE J. Sel. Topics Appl. Earth Observ. Remote Sens.*, vol. 7, no. 1, pp. 327–339, Jan. 2014.

[24] L. Zhang, L. Zhang, D. Tao, and X. Huang, "Tensor discriminative locality alignment for hyperspectral image spectral–spatial feature extraction," *IEEE Trans. Geosci. Remote Sens.*, vol. 51, no. 1, pp. 242–256, Jan. 2013.

[25] L. Wang, D. Liu, and Q. Wang, "Geometric method of fully constrained least squares linear spectral mixture analysis," *IEEE Trans. Geosci. Remote Sens.*, vol. 51, no. 6, pp. 3558–3566, Jun. 2013.